Contact-free Nonplanar Haptics with a Spherical Electromagnet

Juan José Zárate[†,1], Thomas Langerak[†,1], Bernhard Thomaszewski[2] and Otmar Hilliges[1]

***Abstract*— In this paper we introduce a novel contact-free volumetric haptic feedback device. A symmetric electromagnet is used in combination with a dipole magnet model and a simple control law to deliver dynamically adjustable forces onto a hand-held tool. The tool only requires an embedded permanent magnet and thus can be entirely untethered. The force, however, while contact-free, remains grounded via the spherical electromagnet and relatively large forces (1N at contact) can be felt by the user. The device is capable of rendering both attracting and repulsive forces in a thin shell around the electromagnet. We report findings from a user experiment with 6 participants, characterizing force delivery aspects and perceived precision of our system. We found that users can discern at least 25 locations for repulsive forces.**

I. Introduction

Many emerging computing paradigms such as virtual and augmented reality (VR/AR) rely on haptic feedback as an additional information channel to improve the user experience. For example, in VR, haptic feedback increases the sense of presence and immersion by rendering collisions, shapes, and forces between the user and virtual objects.

Existing approaches either rely on vibro-tactile actuators that are embedded into handheld controllers, displays or worn on the body. Such actuators can only render coarse, non-localized haptic sensations. More complex setups such as articulated arms and exoskeletons can render both large-force haptic feedback and can operate in three-dimensional space, but typically require force anchoring in the environment and require complex, and often bulky mechanisms, which prevents walk-up-and-use scenarios, thus hindering user uptake.

To address this challenge, we propose an approach to deliver contact-free, volumetric haptic feedback via an omni-directional electromagnet. The device consists of a single 60 mm diameter spherical electromagnet and can render attractive and repulsive forces onto permanent magnets embedded in pointing tools such as a stylus or magnets directly worn on the user's fingertip. Leveraging a dipole-dipole approximation of the electromagnet-magnet interaction, our system is capable of calculating and controlling the forces exerted onto the permanent magnet in real-time while dynamically adjusting the force that is perceived by the user. The system can deliver perceptible forces up to 1N in a thin volume above the surface. Furthermore we demonstrate that users can distinguish at least 25 different set-points separated by 18° on the surface of the sphere.

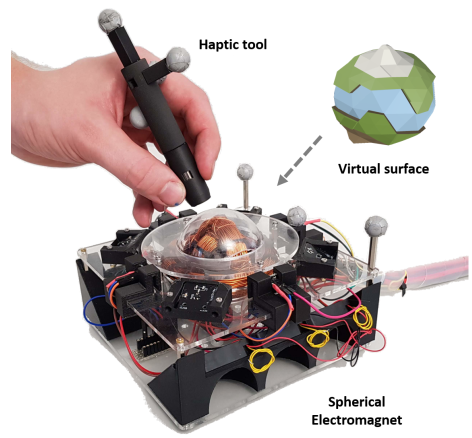

Fig. 1. We introduce a novel contact-free mechanism to render haptic feedback onto a tracked stylus via a hemispherical electromagnet. An approximate model of the magnet interaction and a computationally efficient control strategy allow for the dynamic rendering of attracting and repulsive forces, for example, allowing users to explore virtual surfaces in a thin shell surrounding the device (inset).

To demonstrate the efficacy of our approach we designed a functional prototype comprising of an iron core and three custom wound copper coils. The electromagnet is encased in a plastic dome upon which tools can come into contact and move about its surface (see Figure 1). The prototypical system can render radial (along the vector from the magnet to the tool) and tangential forces, both in the attractive and repulsive polarity. The system can furthermore dynamically adjust the opening angle and steepness of the electromagnetic potential to gently guide the user towards a desired set-point in the thin volume above the device.

Modulating the magnetic field as a function of tool position opens the door to many different interactive applications. In a virtual terrain exploration, the tool can be repelled when moved along mountains and attracted to valleys while descending (see Figure 1, inset). As another example, the sensation of stirring a viscous liquid may be created by emulating the drag of the fluid on the tool. To enable these interactive experiences, our device builds on three key components that represent our contributions in this work:

- A computational model based on magnetic dipole-dipole interaction to produce force maps that allow for designing and generating location-dependent feedback,
- The design and implementation of a 3 degree-of-

[†]Authors contributed equally to this work.

[1]J.J. Zarate, T. Langerak and O. Hilliges are with the AIT Lab, Department of Computer Science, ETH Zurich, 8092 Zurich, Switzerland. juan.zarate, thomas.langerak, otmar.hilliges @inf.ethz.ch

[2]B. Thomaszewski is with Université de Montréal, Department of Computer Science and Operations Research, Montreal, QC, Canada. bernhard@iro.umontreal.ca

freedom (DoF) spherical electromagnet prototype,
- A control strategy that translates desired high-level forces into low-level input signals (currents/voltages) for the coils, fast enough for interactive use.

To assess the efficacy of the proposed design we characterize the system properties experimentally and report findings from a perceptual study which explores the thresholds for perception and localization capabilities of the electromagnetic actuation approach. Results from these early user tests indicate that users can perceive at least 25 different spatial locations with high precision.

A. Related work

VR and wearable computing have seen rapid adaptation of haptics in recent years. Many such systems leverage vibrotactile actuators for feedback. These are often embedded into hand-held controllers (e.g., HTC Vive), directly into displays [1] or are worn on the body [2], [3]. Vibro-tactile actuation however can only render coarse, non-localized sensation. More complex setups often involving articulated arms or external braking mechanisms [4]–[8] can reproduce higher fidelity haptics and render both tactile and kinesthetic feedback. Similarly, exoskeletons and gloves [9]–[11], or tilt platforms [12], [13] can produce large forces. These type of grounded approaches however require anchoring of the force in the environment requiring complex mechanical structures and adding bulk. As a result, they are mostly limited to use in high-end niches such as robotic surgery and tele-operation.

Recently much work has focused on providing rich, yet contact free haptic feedback, overcoming the need for expensive and complex robotic-arm like elements [14]. Many different actuation principles have been explored, including active motion control of the tip of a hand-held stylus [15], ultra-sound pressure waves [16], and even drone-based delivery of haptics [17]. However, by far the most practical way to provide contact-free haptics is via the use of magnetism. In the simplest case this can be achieved via integration of passive magnets into interactive objects, for example via 3D printing [18], [19], sometimes such approaches can be combined with sensing capabilities [20]. However, relying on permanent magnets does not allow any dynamic control over the perceived forces.

Electromagnets (EM) allow for computational control of the forces (and sometimes torques) and have been used to create planar EM arrays to interactively attract or repulse magnets embedded into styluses or directly worn on the user's finger [21]–[26]. Electromagnetism has also been exploited to deliver contact-free vibration onto a magnet in a 3D pointing device [27]. Moreover, leveraging the Lorentz force to actuate a coil between two permanent magnets can deliver precise and large mechanically grounded forces onto a joystick [28]. However, range-of-motion is limited and the handheld grip has to be mechanically connected to the powered coil, rendering contact-free haptics infeasible.

Possibly the closest related work to ours are the Omnimagnet by Petruska et al. [29] and its variants [30]. Like ours, the system generates an omni-directional magnetic field in the surroundings of the actuator. However, the design is composed of 2-3 nested cuboid coils, which causes rapid force decay as the user moves along the surface of the device. Furthermore, the construction complicates heat dissipation and thus limits the maximal strength and duration of generated forces [31], making it most suitable for rendering of vibrotactile stimuli onto a stylus in a fixed position [32]. Furthermore, these devices rely on a cubical design. That means the center-to-center distance (d) between the two magnets inevitably must vary as the user explores the surface. This translates into high variance of the forces due to the quartic decay with distance (i.e., $F \propto 1/d^4$). Our design is spherical, symmetric and, to the best of our knowledge, for the first time demonstrates rendering of symmetric, contact-free continuous forces inside a partial spherical shell, of $\pm 60^\circ$. We also propose a control algorithm that allows for dynamic shaping of the perceived force depending on the hand-held tool's position in 3D space.

II. System Description

We introduce a haptic feedback system that enables dynamic interactions with virtual surfaces through an untethered, contact-free tool. Our device is a hemispherical shell. The core consists of three coils with mutually orthogonal axes. By controlling the current flow through the coils, we are able to shape the magnetic field around the device. This, in turn, enables the device to exert controlled electromagnetic forces on the permanent magnet located inside a hand-held tool such as a stylus. Despite being contact-free, the forces perceived by the user are ultimately grounded to the support onto which the device is mounted, allowing for comparatively strong feedback.

We now detail the main components that make up our contribution: 1) a computational model of the electromagnet-magnet interactions; 2) the prototypical hardware design and 3) a real-time control algorithm.

A. Haptic force mapping

To enable the envisioned interactive experiences, we must be able to dynamically adjust the haptic feedback. We therefore require a model for the magnetic interaction between device and tool that is *1)* precise enough to predict forces with sufficient accuracy and *2)* fast enough to run at the feedback rates required for haptic interaction.

Computing the magnetic field around, and resulting interaction between, arbitrarily-shaped objects is a challenging and computationally expensive task. However, even though the magnetic field can be very complex in the direct vicinity of an object, this complexity rapidly decays with increasing distance and approaches a simple dipole field. This fact has been exploited in previous work to construct fast, approximate models based on dipole-dipole interaction [33]. Instead of solving the Maxwell equations on a discretization of ambient space, this approximate model only requires the magnitude and orientation of the magnetic moment of each dipole, leading to drastically reduced computation times.

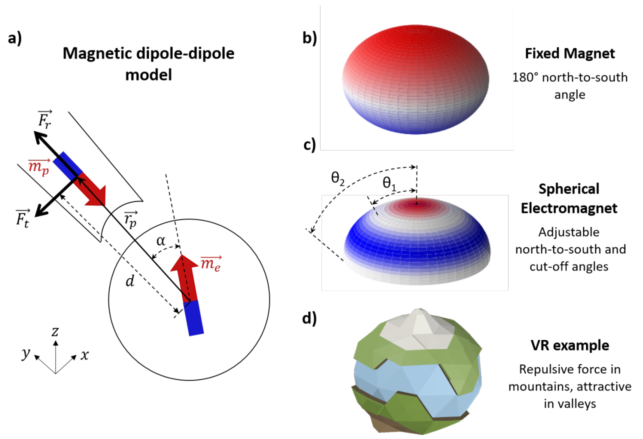

Fig. 2. Schematic of the main quantities necessary to compute desired radial and tangential forces (a). Insets show: force map of a permanent magnet (b). Adjustable force map generated by our approach (c). Here $\mathbf{r_0} = d_{min}\mathbf{e_z}$, $\theta_1 = \pi/10$ and $\theta_2 = 3\pi/10$. Example virtual surface that can be felt by the user (d).

In adopting this approach, we model both the electromagnet of the device and the tool as a single dipole (see Figure 2.a). Let $\mathbf{m_p}, \mathbf{m_e} \in \mathbb{R}^3$ denote the magnetic moments of the permanent magnet in the tool and the electromagnet in the device, respectively. The force exerted on the tool, expressed in local coordinates, are obtained as:

$$\mathbf{F_r} = -\frac{3\mu_0\ m_e\ m_p}{2\pi\ d^4}\cos(\alpha)\ \mathbf{e_r}\ , \quad (1)$$

$$\mathbf{F_t} = -\frac{3\mu_0\ m_e\ m_p}{4\pi\ d^4}\sin(\alpha)\ \mathbf{e_t}\ , \quad (2)$$

where $m_e = |\mathbf{m_e}|$, $m_p = |\mathbf{m_p}|$. In the above expression, $\mathbf{F_r}$ is the force in the radial direction $\mathbf{r_p} = d\ \mathbf{e_r}$ from the center of the device to the tool. Likewise, $\mathbf{F_t}$ is the force in the tangential direction $\mathbf{e_t}$ that tends to align the location of the two dipoles along $\mathbf{e_r}$. Assuming that the tool is in contact with the shell, both force components depend only on the relative angle α between the dipoles. Furthermore, $\mathbf{F_r}$ and $\mathbf{F_t}$ are attractive (negative) when the two dipoles have the same sign and $\alpha < \pi/2$. Conversely, the forces become repulsive (positive) when the dipoles have opposite orientations (see Figure 2.a).

The interaction forces decay quickly, as $1/d^4$, with increasing magnet-magnet distance. The maximum force $\mathbf{F}_{\mathrm{r,max}}$ is obtained when the tool is in contact with the device ($d = d_{\mathrm{min}}$). In our case, $d_{min} = 50$ mm, since the outer case radius is 30 mm and inside the tool, the magnet center is 20 mm away from the tool tip. Our proposed geometry ensures that the distance d will remain constant across the working surface as long as the tool is kept in contact with the surface, allowing for a much simpler control of the force. However, it is worth noting that moving the tool $1cm$ away in the radial direction makes the force fall to approximately $\mathbf{F}_{\mathrm{r,max}}/2$, another extra centimeter results in a force $\mathbf{F}_{\mathrm{r,max}}/4$. This rapid decay of the interaction forces can, to some extent, be mitigated by increasing the intensity of the magnetic field. However, to maintain power consumption and thermal effects within reasonable bounds, we constrain our interactions to a volumetric shell ($d_{min} \leq d \lesssim d_{min} + 2cm$) above the device's surface.

Equations 1 and 2 also reveal the comparatively weak variation of force magnitude with respect to angle that one would expect when two magnets interact: switching from attractive to repulsive forces requires a change in orientation of $\alpha = \pi$; see Figure 2.b. This weak force variation is inherent to permanent magnets: whereas the far-field interaction is dominated by torque (which decays only as $1/d^3$), the near-field force interaction is governed by the location of the dipoles, not their orientation. In our setting, this property would translate into weak angular resolution with a permanent magnet. To address this problem, we introduce the concept of a *force map* that uses magnetic pole transformation to take advantage of the spherical symmetry and that is compliant with the physics of the system. Our system can generate force maps equivalent to multiple alternating pole regions, having sharper repulsive domes and attractive valleys. The force map is defined by four parameters:

- The center $\mathbf{r_0}$ of the potential. When rendering a mountain-like dome, for instance, $\mathbf{r_0}$ is the summit.
- The height of the dome is measured as the maximum magnetic moment intensity m_{e0}.
- The angle (θ_1) (i.e., the location of the tool in polar coordinates wrt to $\mathbf{r_0}$) where the radial force vanishes for the first time. In our example, (θ_1) is the angle from the summit to the base.
- The cut-off angle θ_2 after which the potential is set to be zero. Having such a cut-off mechanism allows us to control how many individual potentials can be combined into one force map without mutual interference.

Figure 3 summarizes our algorithm to calculate the actuation vector $\mathbf{m_e}$ given the tool position and force map as input. For simplicity and efficiency, we perform the different calculations in their natural coordinate system: the Cartesian system $\mathbf{r} = [x, y, z]$, the spherical system relative to the map's center $\mathbf{r_0}$, and the spherical system centered around the tool position $\mathbf{r_p}$.

The force calculation incorporates the angular scaling by using $(\alpha\frac{2\theta_1}{\pi})$ as argument for the trigonometric functions in Equations 1 and 2. Note that if $\theta_1 = \pi/2$, we recover a permanent magnet. In Figure 2.c, we show an example where the center of the potential (*red*) is on the north pole of the sphere, the first vanishing region (*white*) appears at 18° and the forces are cut off at 54° (*blue*).

Using the algorithm described in Figure 3, we obtain at each time step an actuation input $\mathbf{m_e} = (m_{e-x}, m_{e-y}, m_{e-z})^T$ given the tool position. Depending on the requirements of the application, the potential parameters (center position, intensity, angular variation, and cut-off) may also change as a function of tool position. For example, the force map for the terrain example can be dynamically adapted to emulate changes in landscape over time.

Algorithm to calculate desired forces

% To compute $\mathbf{m_e}$ *given the tool position and the force map.*

Function: $calc\_Me\ (\mathbf{r_p}, \mathbf{r_0}, m_{e0}, \theta_1, \theta_2)$:

$\mathbf{r_p}|_{\mathbf{r_0}} = \mathbb{T}_{\mathbf{r}\to\mathbf{r_0}} \cdot \mathbf{r_p}$

$\mathbf{F}|_{\mathbf{r_0}} = calc\_F\ (\mathbf{r_p}|_{\mathbf{r_0}}, \mathbf{r_0}, m_{e0}, \theta_1, \theta_2)$

$\mathbf{F} = (\mathbb{T}_{\mathbf{r}\to\mathbf{r_0}})^{-1} \cdot \mathbf{F}|_{\mathbf{r_0}}$

$\mathbf{F}|_{\mathbf{r_p}} = \mathbb{T}_{\mathbf{r}\to\mathbf{r_p}} \cdot \mathbf{F}$

$\mathbf{m_e}|_{\mathbf{r_p}} = \frac{4\pi d^4}{3\mu_0}\ [1, 1, -1/2] \cdot \mathbf{F}|_{\mathbf{r_p}}$

$\mathbf{m_e} = (\mathbb{T}_{\mathbf{r}\to\mathbf{r_p}})^{-1} \cdot \mathbf{m_e}|_{\mathbf{r_p}}$

return $\mathbf{m_e}$

% To compute the actuation force in the $|_{\mathbf{r_0}}$ *coordinates.*

Function: $calc\_F\ (\mathbf{r_p}|_{\mathbf{r_0}}, \mathbf{r_0}, m_{e0}, \theta_1, \theta_2)$:

$F_r = 0$

$F_t = 0$

if $d < d_{max}$ **and** $\alpha < \theta_2$ **then**

$F_r = 2F_0\ cos(\alpha \frac{2\theta_1}{\pi})\ \left(\frac{||\mathbf{r_0}||}{||\mathbf{r_p}||}\right)^4$

$F_t = F_0\ sin(\alpha \frac{2\theta_1}{\pi})\ \left(\frac{||\mathbf{r_0}||}{||\mathbf{r_p}||}\right)^4$

end if

$\mathbf{F}|_{\mathbf{r_0}} = [F_r, F_t, 0]$

return $\mathbf{F}|_{\mathbf{r_0}}$

Fig. 3. Pseudo-code of our force calculation algorithm. Note that $\mathcal{T}_{r_i \to r_j}$ is the rotation matrix that maps from coordinate system r_i to r_j, and that $\mathbb{T}_{r_j \to r_i} = (\mathbb{T}_{r_i \to r_j})^{-1} = (\mathbb{T}_{r_i \to r_j})^T$.

B. Spherical electromagnetic actuator

Having laid out the computational model for generating haptic feedback based on dipole interactions, we now describe hardware and implementation aspects for rendering these forces on our device (Fig. 1).

Our device renders haptic forces by controlling the magnetic field generated by a spherical electromagnet. Compared to other alternatives, this approach has several advantages. First, there are no mechanically moving parts in the actuator, reducing complexity and eliminating wear. Changing the orientation of the resulting force on the tool is accomplished by adapting the currents in each coil such as to rotate the induced dipole in the core as desired; see also Figure 4. The underlying physical principle is that, in the presence of linear and isotropic materials, the magnetic field $\mathbf{B}(\mathbf{r})$ in any given point $\mathbf{r}$ can be calculated as the sum over all contributions of all magnetic sources [29]. Under this linearity property of $\mathbf{B}$, the magnetic field produced by the three orthogonal coils is the superposition of the fields generated by each coil individually. Finally, we insert a magnetic core with isotropic (i.e., spherical) geometry and material at the center of the coils and operate it in the linear regime (i.e, $m_e << m_{saturation}$), linearity is maintained such that $\mathbf{B}(\mathbf{r})$ can be computed by summing up each coil's contributions.

In order for the previous statement to remain valid, two assumptions have to be made. First, hysteresis effects can be neglected: the lower the coercivity and remanence of the core material, the lower the effect of past states of the electromagnet on the current one. The second assumption is that the distance d between dipoles is large enough such that the core magnetization due to m_p is small compared with the effect of the coils. This will not be true if, for example, the tool snaps to the sphere with no electrical current in the coils. In our setting, however, a spherical cap around the coils prevents too close approach of the tool and, at the same time, provides the grounding required for generating sufficiently strong interaction forces.

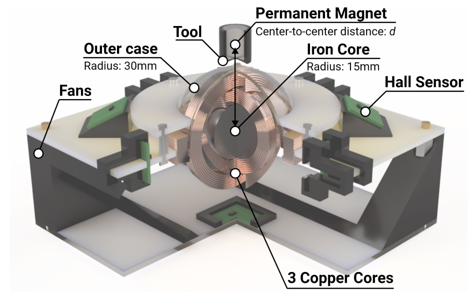

Fig. 4. 3D cross-section of the proposed hardware setup. The device measures 15×15 cm across the base. Three coils are placed, orthogonal to each other and surrounding the iron core. Forces can be rendered onto a permanent magnet moving above the device. Hall sensors are used for calibration. A plastic cover isolates the coils from the user thermally and electrically. Active cooling is provided via several fans mounted in the base.

For the standard low-carbon steel core, we did not observe any hysteresis effects for the update of $\mathbf{m_e}$ at 50 Hz refresh rate. To avoid the undesired self-magnetization of the core due to the tool, we tuned the size of the permanent magnet and the coil parameters using FEM simulations, followed by minor design adjustments informed by real-world test.

The design choices for the hardware of our prototype are motivated by our goal to develop a device that is affordable and easy to manufacture. In particular, we use off-the-shelf electronic components but custom wound coils. FEM simulations in Comsol Multiphysics are used to assist in the exploration of the design space. In Figure 4 we show a 3D CAD rendering of our device. The external dimensions are 150 mm by 150 mm by 95 mm. The structure is built out of laser-cut acrylic glass and 3D-printed parts. The three orthogonal coils are arranged around the $30mm$ steel core. All coils have a resistance of roughly 0.6Ω at room temperature. We use the 12V line of a standard CPU power supply to drive the coils, meaning a maximum electrical current of 24A per coil at full strength. The electrical current in each coil is controlled by a high-power motor driver (Pololu 18v17). The PWM signals are generated by a 12-bit driver (PCA9685) that allows for easy tuning of the carrier frequency and the duty cycle with 12 bit resolution. To be able to accurately control the electrical current and compensate for thermal drifts, we use INA219 current sensors in each coil with a 0.01Ω shunt resistor. Finally, an Arduino board creates the bridge between the I2C components and the PC. The hardware is completed by 9 hall sensors arranged co-linearly

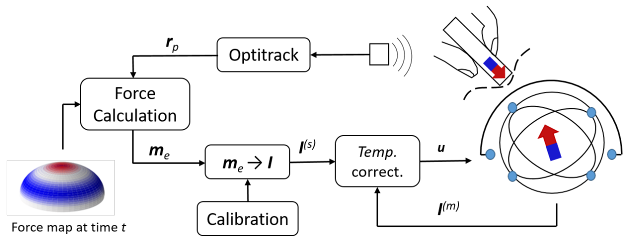

Fig. 5. Schematic overview of the software pipeline. Given the desired force map at time t, and the tool position provided by an external tracking system, we calculate the input value $\mathbf{m_e}$ using the algorithm of Fig. 3. Then the system inputs are computed Eq. 4, and finally a temperature compensation step corrects the system inputs.

with the axes and diagonals of the coils. Six fan coolers below the coils provide active cooling.

C. Control Strategy

The main objective of the actuator control loop is to generate a stable and controllable force on the haptic tool. Although the mathematical principles are straightforward, the practical implementation poses some problems. Since the magnetic field is directly proportional to the current (Fig. 7), controlling the latter is sufficient to determine the state of the system. If the resistance is known, controlling the voltage is equivalent to controlling the current via Ohms law,

$$I = V/R \;, \tag{3}$$

and the voltage in turn can be controlled via Pulse-Width Modulation (PWM). Therefore the input to our system is the PWM frequency. The complete control loop is shown in Figure 5. However, significant heating occurs due to the necessary power that in turn increases the resistance. Therefore the PWM duty cycle (i.e., voltage) needs to be adjusted to maintain a constant current. Measuring the current allows to determine the resistance via inversion of Eq 3. A simple controller then computes an input $\mathbf{u} \in [-1, 1]$ at time t, corresponding to the PWM duty cycle. This depends on the desired current in Ampere ($\mathbf{I}_t^{(s)}$), the resistance in Ohm ($\mathbf{R}_t$) and the maximum voltage in the system, $V_0 = 12$:

$$\mathbf{u}_t = \frac{\mathbf{I}_t^{(s)}}{V_0} * \mathbf{R}_t \quad , \tag{4}$$

where $I_t^{(s)}$ is based on the desired magnetization, $\mathbf{m}_e$, computed via the algorithm presented in Fig. 3 and can be determined via Biot-Savart Law (adapted for our purpose):

$$I_t^{(s)} = \mathbf{c} * \frac{\mathbf{m}_e * \mu_0}{2 * \pi * \mathbf{d}^3} \quad , \tag{5}$$

here $\mathbf{c}$ is a constant coming from a calibration procedure; that, with the help of five hall sensors, maps input current to $\mathbf{m}_e$ (Fig. 7). $\mu_0 = 4 * \pi * 10^{-7}$ is the relative permeability of air and d is the distance from the core to the hall sensors used for calibration (0.055 meter). Due to the thermal effects $\mathbf{R_t}$ however is not a constant, but depends on the measured current ($\mathbf{I}_t^{(m)}$) computed and averaged over a sliding window:

$$\mathbf{R}_t = \frac{V_0 * \frac{1}{N} \sum^N \mathbf{u}_{t-i}}{\frac{1}{N} \sum^N \mathbf{I}_{t-i}^{(m)}} \quad . \tag{6}$$

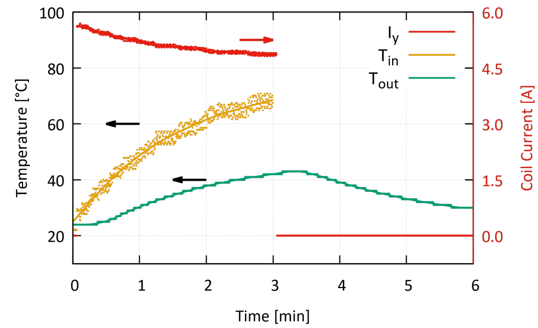

Fig. 6. Thermal characterization of one of the coils as function of time. During the first 3 minutes the y-coil is driven with PWM=30%, and then we let it cool over the remaining 3 minutes. T_{in} is calculated by taking the thermally caused resistance variations into account while the current I_y is 'on', and T_{out} is measured.

III. System Evaluation

One of the main physical limitations of EM-based systems are thermal effects due to Joule heating, to obtain large forces [31]. The temperature is directly proportional to the actuation power (P), and the thermal dissipation obtained by the active and/or passive cooling. We evaluated the thermal behaviour of our system for different power values. In this experiment, we set the current to 'on' for three minutes and then let the device cool down. Figure 6 shows data from the middle coil actuated at PWM = 30%. T_{out} is the temperature measured at the coil boundary, measured with a *Dallas DS18B20* sensor. T_{in} is the average temperature of the copper wire obtained via the variation in resistance. We also plot the electrical current I_y that drops as the coil heats up and the resistance increases. Note that no temperature compensation was used for building these thermal calibration curves. Each coil is able to accumulate some heat during the actuation and continuously dissipates it by the forced air circulation. Our system has a thermal time (τ_T) in the order of minutes, in which it reaches the asymptotic temperature. The average power in the past τ_T seconds must be maintained within a safe value P_{ave}. Based on this plot, we choose $P_{ave} = 17W$ per coil for our system. However, each coil can absorb peaks up to $15 * P_{ave}$ for a few seconds.

Within this safe range, we calibrate the values of m_e for each axis as a function of the current in each coil with the hall sensors around the sphere (see Figure 4) and with Eq. 5. Figure 7 shows the experimentally attained magnetization in the core $\mathbf{m_e}$ as a function of the current. For reference, applying a power $P_0 = 100$ W to each coil ($I_i = 12.9$ A), the equivalent dipole is $\mathbf{m_e} = [2.52; 2.7; 2.82]$ Am^2. We also obtain non-zero terms away from the diagonal since the coils are not perfectly orthogonal and we use the calibration data to correct the PWM duty cycles.

Finally values for the force acting on the permanent

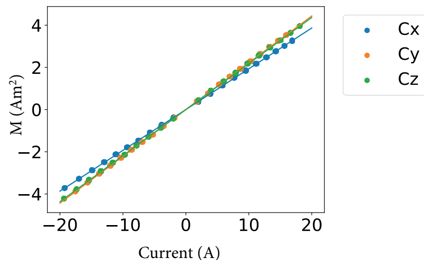

Fig. 7. Electromagnet induced magnetization in each axis, $\mathbf{m_e} = (m_{e-x}, m_{e-y}, m_{e-z})$, as a function of the applied current settings (I_x, I_y, I_z). The magnetic field values are measured with hall sensors placed co-linear with each coil, and then transformed into M values.

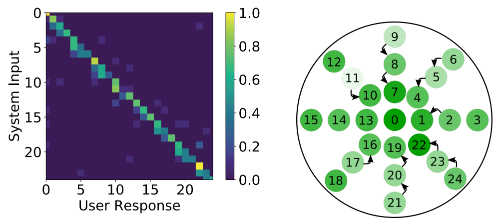

Fig. 8. *Left:* confusion matrix of the 25 set-points, averaged over all users. High values on the diagonal indicate little confusion and the ability to differentiate between different set-points. *Right:* Set-points used in the study. The opacity directly correlates with the percentage of correct identifications by the users. Arrows are drawn when 33% or more of the *wrong* answers were attributed to set-point that the arrow points to.

magnet can be attained via setting the magnetic dipole of the tool and Eq. 1 and 2. In our experiments we use a ring-shaped neodymium magnet (12 mm outside diameter, 5 mm inside diameter, 24 mm high). For any tool with this particular magnet, with a center to center distance between dipoles of 5 cm, we obtain a ratio of force per electrical current of 48 mN/A. This means the device can handle an averaged constant force of $F_r = 258$ mN ($P = 17$ W) with a peak force of up to $F_r = 959$ mN ($P = 230$ W) at full strength (using PWM control). This force value can be increased by increasing the volume of the tool magnet, with the trade-off of loosing angular resolution and adding weight to the tool.

IV. User Evaluation

To assess the efficacy of our proposed approach we validate the prototype in a perceptual study with 6 participants in order to 1) determine how well users can differentiate between different set-points, and 2) how accurate and precise users are with finding a set-point.

Procedure: Based on an pilot study we predetermine 25 evenly seperated set-points (Figure 8 right). We randomly selected a set-point, asked the user to find it, and report the corresponding number. Upon reporting we also measured the euclidean distance to actual set-point. Every set-point was prompted exactly twice, resulting in 50 data points per user (300 in total). Only repulsive forces were tested. We used the same mapping parameters as in Figure 2.

Location accuracy: Figure 8 depicts the resulting confusion matrix between set-points. It can be seen that users accurately perceive discrete actuation points. For those actuation points

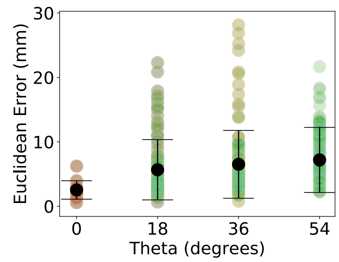

Fig. 9. Euclidean distance between the true set-point position and the user reported position as a function of the azimuth (θ), measured from the top of the sphere and averaged over all angles and users.

that do cause incorrect answers, users tend to pick the neighboring location (typically higher on the sphere). This effect is pronounced along the meridian arc facing away from the user, whereas the orthogonal meridian produces less erroneous detections. This could be due to the position of the hand and arm and differences in muscle groups that are involved in actuating the wrist versus the whole hand. The difference in coil diameters could be another contributing factor.

Precision: we report the precision with respect to the angle θ. Figure 9 shows that the error increases as a function of the angle. A potential contributing factor here is that gravity has more impact on the pen the further down it moves on the hemisphere. This may make it more difficult for users to differentiate the the em-actuation force and gravity. The mean errors of $2.5mm \pm 1.4$, $5.7mm \pm 4.6$, $6.5mm \pm 5.2$ and $7.2mm \pm 5.1$ are relatively small across the device.

V. Discussion & Conclusion

In this paper we presented a novel contact-free volumetric haptic feedback device. A symmetric electromagnet is used in combination with a dipole magnet model and a simple control law to deliver dynamically adjustable forces onto a hand-held tool such as a stylus. The tool only requires an embedded permanent magnet and can be entirely untethered. The force however remains grounded via the electromagnet and hence relatively large forces can be felt by the user.

Despite many advantages, the proposed method also has drawbacks. Heat generation limits the number of interactions that are possible within a certain time frame. Furthermore, when driving the system at full power, continuous interaction is limited to 5 seconds. However, at a PWM cycle of 50% the interaction can be extended to a minute.

It is also important to note that interaction between magnets involves not only forces but also torques. In this work we focused on the control of the three force components via the 3 DoFs of the electromagnet. In this case, the torque values will adapt to satisfy these conditions. However, the same procedure outlined here can be applied to control for a specific torque map (leaving the force values unconstrained), or a combination of force and torque.

In future work, we want to explore the dynamic capabilities of our proposed approach including more advanced control schemes to continuously shape the force map.

ACKNOWLEDGMENT

This work was supported in part by an ERC starting grant (OPTINT) grant agreement No 803491.

REFERENCES

[1] P. Wellman and R. D. Howe, "Towards Realistic Vibrotactile Display in Virtual Environments," in *Proceedings of the ASME Dynamic Systems and Control Division*, 1995, pp. 713–718.

[2] CyberGlove Systems Inc., "CyberTouch Glove," http://www.cyberglovesystems.com/cybertouch, last accessed: 18.03.2017.

[3] NeuroDigital Technologies, "Gloveone Glove," https://www.neurodigital.es/gloveone/, last accessed: 29.03.2017.

[4] T. H. Massie and J. K. Salisbury, "The PHANToM Haptic Interface: A Device for Probing Virtual Objects," in *Proceedings of the ASME Winter Annual Metting '94*, ser. Dynamics and Control 1994, 1994, pp. 295–301.

[5] R. E. Stamper, "A Three Degree Of Freedom Parallel Manipulator With Only Translational Degrees Of Freedom," Ph.D. dissertation, University of Maryland at College Park, 1997.

[6] R. Q. Van Der Linde, P. Lammertse, F. E., and R. B., "The HapticMaster, a new highperformance haptic interface," in *Proceedings of Eurohaptics 2002*, 2002.

[7] B. Araujo, R. Jota, V. Perumal, J. X. Yao, K. Singh, and D. Wigdor, "Snake Charmer: Physically Enabling Virtual Objects," in *Proceedings of the TEI '16: Tenth International Conference on Tangible, Embedded, and Embodied Interaction*, ser. TEI '16. New York, NY, USA: ACM, 2016, pp. 218–226. [Online]. Available: http://doi.acm.org/10.1145/2839462.2839484

[8] E. I. Zoller, P. C. Cattin, A. Zam, and G. Rauter, "Assessment of the functional rotational workspace of different grasp type handles for the lambda. 6 haptic device," in *2019 IEEE World Haptics Conference (WHC)*. IEEE, 2019, pp. 127–132.

[9] CyberGlove Systems Inc., "CyberGrasp Glove," http://www.cyberglovesystems.com/cybergrasp, last accessed: 12.03.2017.

[10] X. Gu, Y. Zhang, W. Sun, Y. Bian, D. Zhou, and P. O. Kristensson, "Dexmo: An Inexpensive and Lightweight Mechanical Exoskeleton for Motion Capture and Force Feedback in VR," in *Proceedings of the 2016 CHI Conference on Human Factors in Computing Systems*, ser. CHI '16. New York, NY, USA: ACM, 2016, pp. 1991–1995. [Online]. Available: http://doi.acm.org/10.1145/2858036.2858487

[11] I. Choi and S. Follmer, "Wolverine: A Wearable Haptic Interface for Grasping in VR," in *Proceedings of the 29th Annual Symposium on User Interface Software and Technology*, ser. UIST '16 Adjunct. New York, NY, USA: ACM, 2016, pp. 117–119. [Online]. Available: http://doi.acm.org/10.1145/2984751.2985725

[12] D. Prattichizzo, F. Chinello, C. Pacchierotti, and M. Malvezzi, "Towards Wearability in Fingertip Haptics: a 3-DoF Wearable Device for Cutaneous Force Feedback," *EEE Trans. Haptics*, vol. 6, no. 4, pp. 506–516, Oct 2013. [Online]. Available: http://dx.doi.org/10.1109/TOH.2013.53

[13] H. Kim, M. Kim, and W. Lee, "HapThimble: A Wearable Haptic Device Towards Usable Virtual Touch Screen," in *Proceedings of the 2016 CHI Conference on Human Factors in Computing Systems*, ser. CHI '16. New York, NY, USA: ACM, 2016, pp. 3694–3705. [Online]. Available: http://doi.acm.org/10.1145/2858036.2858196

[14] J. B. Brink, A. J. Petruska, D. E. Johnson, and J. J. Abbott, "Factors affecting the design of untethered magnetic haptic interfaces," in *2014 IEEE Haptics Symposium (HAPTICS)*. IEEE, 2014, pp. 107–114.

[15] S. Kianzad and K. E. MacLean, "Harold's purple crayon rendered in haptics: Large-stroke, handheld ballpoint force feedback," in *2018 IEEE Haptics Symposium (HAPTICS)*. IEEE, 2018, pp. 106–111.

[16] T. Hoshi, M. Takahashi, T. Iwamoto, and H. Shinoda, "Noncontact tactile display based on radiation pressure of airborne ultrasound," *IEEE Transactions on Haptics*, vol. 3, no. 3, pp. 155–165, 2010.

[17] S. Heo, C. Chung, G. Lee, and D. Wigdor, "Thor's hammer: An ungrounded force feedback device utilizing propeller-induced propulsive force," in *Proceedings of the 2018 CHI Conference on Human Factors in Computing Systems*. ACM, 2018, p. 525.

[18] C. Zheng, J. Kim, D. Leithinger, M. D. Gross, and E. Y.-L. Do, "Mechamagnets: Designing and fabricating haptic and functional physical inputs with embedded magnets," in *Proceedings of the Thirteenth International Conference on Tangible, Embedded, and Embodied Interaction*. ACM, 2019, pp. 325–334.

[19] M. Ogata, "Magneto-haptics: Embedding magnetic force feedback for physical interactions," in *The 31st Annual ACM Symposium on User Interface Software and Technology*. ACM, 2018, pp. 737–743.

[20] H.-C. Kuo, R.-H. Liang, L.-F. Lin, and B.-Y. Chen, "Gaussmarbles: spherical magnetic tangibles for interacting with portable physical constraints," in *Proceedings of the 2016 CHI Conference on Human Factors in Computing Systems*. ACM, 2016, pp. 4228–4232.

[21] M. Weiss, C. Wacharamanotham, S. Voelker, and J. Borchers, "Fingerflux: near-surface haptic feedback on tabletops," in *Proceedings of the 24th annual ACM symposium on User interface software and technology*. ACM, 2011, pp. 615–620.

[22] Q. Zhang, H. Dong, and A. El Saddik, "Magnetic field control for haptic display: system design and simulation," *IEEE Access*, vol. 4, pp. 299–311, 2016.

[23] J. Yamaoka and Y. Kakehi, "depend: augmented handwriting system using ferromagnetism of a ballpoint pen," in *Proceedings of the 26th annual ACM symposium on User interface software and technology*. ACM, 2013, pp. 203–210.

[24] A. Adel, M. Mansour, M. M. Micheal, A. Abdelmawla, I. S. Khalil, and S. Misra, "Magnetic localization for an electromagnetic-based haptic interface," *IEEE Magnetics Letters*, vol. 10, pp. 1–5, 2019.

[25] P. Berkelman, M. Miyasaka, and J. Anderson, "Co-located 3d graphic and haptic display using electromagnetic levitation," in *2012 IEEE Haptics Symposium (HAPTICS)*. IEEE, 2012, pp. 77–81.

[26] P. Berkelman, S. Bozlee, and M. Miyasaka, "Interactive rigid-body dynamics and deformable surface simulations with co-located maglev haptic and 3d graphic display," 2013.

[27] J. McIntosh, P. Strohmeier, J. Knibbe, S. Boring, and K. Hornbæk, "Magnetips: Combining fingertip tracking and haptic feedback for around-device interaction," in *Proceedings of the 2019 CHI Conference on Human Factors in Computing Systems*, ser. CHI '19. New York, NY, USA: ACM, 2019, pp. 408:1–408:12. [Online]. Available: http://doi.acm.org/10.1145/3290605.3300638

[28] P. Berkelman and M. Dzadovsky, "Extending the motion ranges of magnetic levitation for haptic interaction," in *World Haptics 2009-Third Joint EuroHaptics conference and Symposium on Haptic Interfaces for Virtual Environment and Teleoperator Systems*. IEEE, 2009, pp. 517–522.

[29] A. J. Petruska and J. J. Abbott, "Omnimagnet: An omnidirectional electromagnet for controlled dipole-field generation," *IEEE Transactions on Magnetics*, vol. 50, no. 7, pp. 1–10, 2014.

[30] P. Berkelman, B. Tix, and H. Abdul-Ghani, "Electromagnetic position sensing and force feedback for a magnetic stylus with an interactive display," *IEEE Magnetics Letters*, vol. 10, pp. 1–5, 2018.

[31] F. Esmailie, M. S. Cavilla, and T. A. Ameel, "A thermal transient model of heat transfer within an omnimagnet," in *ASME 2017 International Mechanical Engineering Congress and Exposition*. American Society of Mechanical Engineers Digital Collection, 2017.

[32] R. Zhang, A. J. Boyles, and J. J. Abbott, "Six principal modes of vibrotactile display via stylus," in *2018 IEEE Haptics Symposium (HAPTICS)*. IEEE, 2018, pp. 313–318.

[33] B. Thomaszewski, A. Gumann, S. Pabst, and W. Straßer, "Magnets in motion," in *ACM Transactions on Graphics (TOG)*, vol. 27, no. 5. ACM, 2008, p. 162.